Commercially derived versatile optical architecture for two-photon STED, wavelength mixing and label-free microscopy

CHIARA PERES,[1,2] CHIARA NARDIN,[1] GUANG YANG,[3] AND FABIO MAMMANO[1,2,3,*]

[1]*CNR Institute of Biochemistry and Cell Biology, 00015 Monterotondo, Rome, Italy*
[2]*Department of Physics and Astronomy "G. Galilei", University of Padova, 35131 Padova, Italy*
[3]*Shanghai Institute for Advanced Immunochemical Studies, ShanghaiTech University, 201210 Shanghai, China*
[*]*fabio.mammano@unipd.it*

Abstract: Multimodal microscopy combines multiple non-linear techniques that take advantage of different optical processes to generate contrast and increase the amount of information that can be obtained from biological samples. However, the most advanced optical architectures are typically custom-made and often require on-site adjustment of optical components performed by trained personnel for optimal performance. Here, we describe a hybrid system we built based on a commercial upright microscope. We show that our multimodal imaging platform can be used to seamlessly perform two-photon STED, wavelength mixing and label-free microscopy in both *ex vivo* and *in vivo* turbid samples. The system is stable and endowed with remote alignment hardware that ensures long-term operability also for non-expert users, using the alignment protocol described in this article and in the related material. This optical architecture is an important step forward towards a wider practical applicability of non-linear optics to bioimaging.

1. Introduction

Imaging methods based on non-linear optical processes offer a combination of high contrast and sub-cellular resolution even in strongly scattering biological tissues, making them suitable for both *in vivo* and *ex vivo* applications [1]. To exploit non-linear imaging processes in thick biological samples, the use of pulsed near-infrared (IR) excitation light is commonplace, because it allows high tissue penetration with low phototoxicity due to reduced photo-absorption [2–4]. In addition, non-linear process are excited mainly in the perifocal zone, implying intrinsic optical sectioning and reduced photodamage above and below the focal plane [5,6]. Non-linear microscopy allows flexible and non-invasive analysis in living tissues close to physiological condition, with high spatiotemporal resolution [7]. Moreover, different non-linear optical processes require similar pulsed near-IR sources [8], making feasible, although not straightforward, to implement multiple imaging modalities in the same microscopy platform.

Second and third harmonic generation (SHG, THG, respectively) [3,4] are among the most widely used label-free non-linear imaging modalities. Harmonic generation is a coherent scattering process with no photon absorption, in which two (or more) photons interact with the sample to generate a photon of exactly half (for SHG) or one third (for THG) of the incoming wavelength. SHG is a particular case of sum frequency generation (SFG) in which the two photons have the same energy [9] and is due to lack of inversion symmetry in the sample. The signal is typically generated by non-centrosymmetric molecules spatially aligned so as to add contributions and generate contrast. SHG is commonly used to investigate collagen fibers of skin and bone, myosin in muscles and microtubules [10,11]. THG depends on the discontinuity of third-order non-linear susceptibility typical of interfaces where refractive index mismatch occurs,

allowing label free imaging of, for example, cell membranes, vessels, lipids and nuclei [12,13]. Another popular label-free imaging modality is coherent anti-stokes Raman scattering (CARS), that is based on molecular vibrational spectroscopy and allows selective non-invasive imaging by detection of specific chemical bond types providing molecular fingerprinting [14]. Over the past years, CARS has increased its popularity as valuable imaging method in the biomedical field, applied for example to imaging of lipids in biological samples and to drug and/or cancer cell identification [15].

The most widely used non-linear method for biological fluorescence imaging is two-photon excitation (2PE) (laser scanning) fluorescence microscopy (FM) [2], which has allowed tissue penetration up to 1.6-mm of depth in the mouse cortex [16]. In 2PE, two photons interact with the sample within ∼5 fs to promote the fluorophore under investigation from the ground state to an excited state. The excited molecule then emits a photon along the normal fluorescence emission pathway [17]. It is also possible to mix two IR excitation wavelengths for two-color two-photon excitation fluorescence microscopy (2c-2PEFM) which enables rapid multicolor 2PE of up to 3 fluorophores with efficient and independent control of the intensity of each fluorescence signal [18]. In 2c-2PEFM, two different pulsed femtosecond lasers are carefully synchronized and spatially aligned so that the 2PE process can be promoted by either one of the two sources as well as by their combination.

The substantially increased tissue penetration reached by two- [16] and three-photon microscopy [19], compared to single-photon excitation (1PE), comes at the expenses of spatial resolution due to the diffraction limit. Indeed, the use of IR light to elicit fluorescence almost doubles the linear dimensions of the excitation point spread function (PSF) compared to confocal one-photon imaging [5]. In order to improve the resolution of 2PEFM, in 2009 Moneron and Hell superimposed a donut-shaped STimulated Emission Depletion (STED) beam on the 2PE excitation beam, thus generating the first 2PE-STED architecture [20]. This mixed modality was used initially for super-resolution imaging in cell monolayers to disclose, for example, fine structure of GFP-tagged fixed cells [21]. However, the full potential of 2PE-STED become appreciable only when imaging fine structures in thick turbid tissue, where the 2PE advantages can be exploited. Thus, 2PE-STED was used, for example, to perform super-resolution imaging of the morphology of dendritic spines [22,23] and of synapses and glial cells in living brain slices [24], or to quantitatively analyze dendritic spine morphology in a living mouse brain [25]. A subsequent implementation improved 2PE-STED performance by using a CW-STED laser, time-resolved detectors and the SPLIT principle to discard non super-resolved photons [26]. To improve stability, a 2PE-STED system based on electrically controlled optical components, called "advanced easySTED", was implemented based on a simplified and more compact architecture [27]. However, none of the two above architectures was tested for 2PE-STED imaging of thick biological samples.

Although near-IR excitation and depletion wavelengths are ideal for deep-imaging in scattering samples, optical aberrations can severely limit 2PE-STED resolution. To compensate for system- and sample-induced aberrations that may affect the quality of the STED beam PSF, the use of adaptive optics (AO) may be beneficial, particularly in turbid media. In this vein, it was implemented a system capable to perform 3D-STED 164 μm deep in fixed mouse brain and 76 μm deep in the brain of a live mouse, by combining 2PE, water-immersion objective and wave-front sensing-based AO system for aberration correction [28]. Recently, another system performed 3D-STED imaging 90 μm deep in acute brain slices using an AO method based on the measurement of optical aberrations as a function of depth in a phantom sample with adjusted refractive index [29]. However, these AO approaches require iterative sample measurements or *a priori* knowledge of the scattering properties of the sample and insertion of programmable components in the optical path, thus increasing system complexity. Moreover, current multimodal or 2PE-STED microscopes, such as those quoted above, were based on custom-made architectures

that require on-site maintenance by trained personnel [30]. To our knowledge, commercial multimodal 2PE-STED microscopes are not available.

Here, to partially fill this gap, we report the implementation of a reliable multimodal imaging platform derived from a commercial upright microscope to perform 2PEF, 2PE-STED, 2c-2PEF, SFG and CARS microscopy in *ex vivo* and *in vivo* samples. To ensure serviceableness also for non-expert users, we endowed the platform with a system for remote alignment of critical opto-mechanical components that allows long-term operability of the platform with no need of frequent on-site intervention for alignment. This optical architecture is an important step forward towards a more user-friendly multimodal microscope that can widen the practical applicability of non-linear optics to microscopy users interested in addressing biological questions *in vivo*.

2. Methods

2.1. Optical architecture

The system described here (Fig. 1(A), 1(B), 1(C), 1(D)) was based on a custom-made Leica TCS SP8 upright multi-photon excitation scanning laser microscope (Leica Microsystem, Wetzlar, Germany). The latter was designed for deep-tissue *in vivo* imaging and was optimized to perform three-dimensional super-resolution microscopy by one-photon STED (1PE-STED). The IR laser source serving the microscope was a tunable femtosecond pulsed Titanium Sapphire (Ti:Sa) Chameleon Ultra II Laser (Coherent, Santa Clara, CA, USA) with output range from 680 nm to 1080 nm. To mitigate group delay dispersion (GDD), which severely limits the performance of any two-photon system, the Ti:Sa laser hosted a negative pre-chirping unit to compensate for ultra-short pulses broadening due to propagation through thick scattering samples. The Ti:Sa laser was coupled to a MPX, Chameleon Compact Optical Parametric Oscillator (OPO) (Coherent) to extend the range of excitation wavelengths. The OPO provided two beam outputs: Ti:Sa output, 680-1080 nm and OPO output, 1000-1340 nm. Each output was pulsed at 80 MHz, with the OPO train pulses delayed by approximately 5.54 ns relative to Ti:Sa pulses as measured at the source output. Each beam, after reflection off silver mirrors, was separately launched into an electro optical modulator (EOM) (Qioptic, Waltham, MA, USA) for fast beam shuttering in the MHz frequency range. Out of the EOM, the combination of a $\lambda/2$ plate mounted in a rotary motorized holder, followed by a polarizing beam splitter (PBS) was used to modulate the intensity of each beam. Collimation and diameter of the Ti:Sa beam were controlled by inserting a $1.2\times$ beam expander (BE) formed by a pair of achromatic doublets with 60 mm and 50 mm focal lengths, respectively (AC254-060-B and AC254-050-B-ML, Thorlabs Inc., NJ, USA). With these focal lengths, the beam filled completely the back focal aperture of the water immersion objective (HC IRAPO L25×/1,00 W motCORR, Leica). To compensate for the nanosecond delay mentioned above, the Ti:Sa beam was directed towards an optical delay line, composed of a pair of silver mirrors mounted in a retro-reflector configuration on a high-precision motorized linear stage (8MTL1401-300-LEn1-100, STANDA, Vilnius, Lithuania). This device enabled computer-controlled sub-micrometric variations of the optical path length, i.e. temporal delay adjustments with a precision in the order of 5 fs. This level of accuracy was essential to perform (i) wavelength mixing and (ii) STED with fluorophores excited by either IR excitation source as detailed in the Results and discussion section.

The OPO beam was steered by using two remotely controlled piezo kinematic mirrors (POLARIS-K1S2P, Thorlabs Inc.; see Figure S1), each coupled with an open loop piezo controller (MDT693B, Thorlabs Inc.). Beam steering was essential for spatial alignment with the Ti:Sa beam after beam merging with a short pass dichroic mirror (SP1035, Leica). Before merging, each beam passed through a half wave-plate mounted on a remotely controlled rotary support. The merged beams impinged on a Glan polarizing prism (GPP, part number PGL 10.2, Bernhard Halle Nachfl. GmbH, Berlin, Germany) used to divert a fraction of the light towards a beam profiler (Grenouille 8-50-USB, Swamp Optics LLC, USA) and a high speed
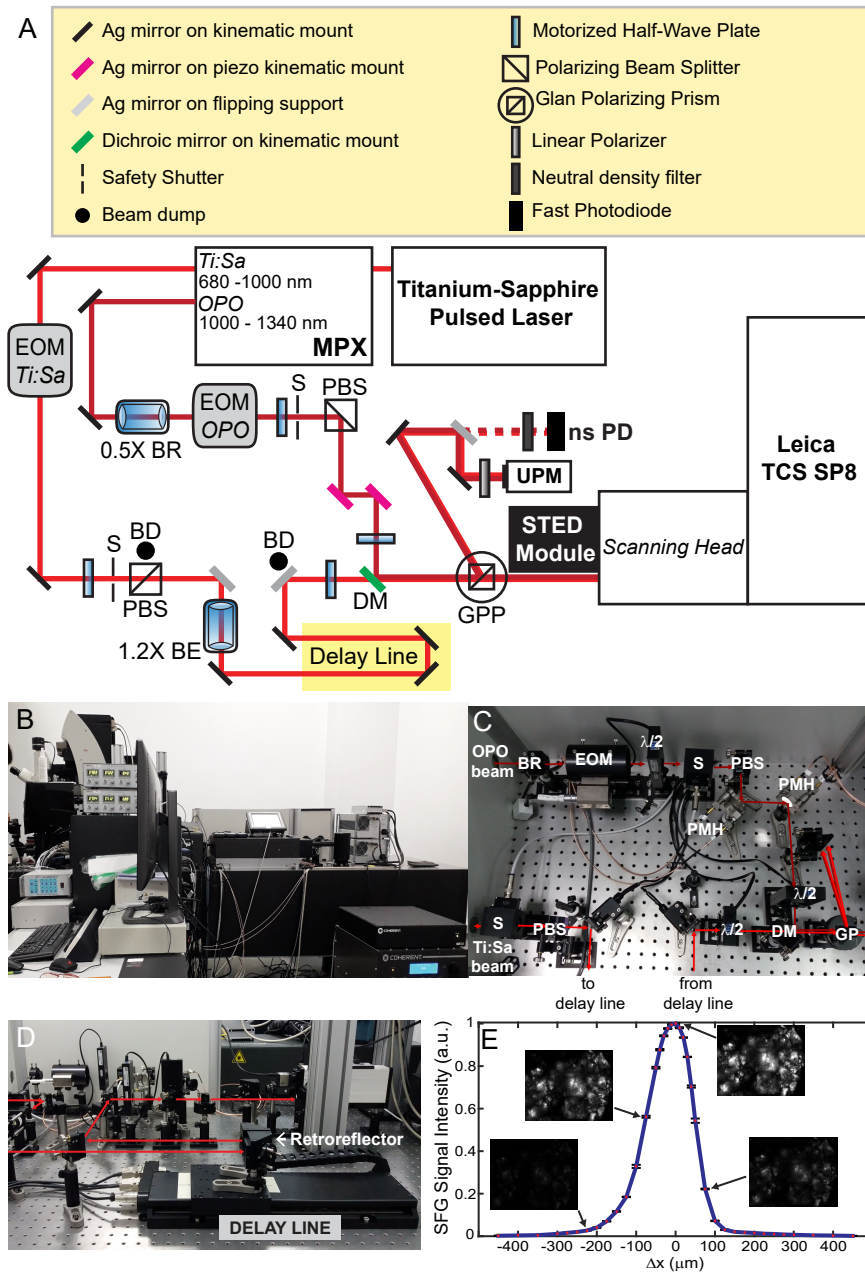
Fig. 1. System description. **A**, Simplified optical scheme: Ag: Silver Mirror; EOM: Electro-Optic Modulator; PBS: Polarizing beam splitter; GPP: Glan Polarizing Prism; BE Beam Expander; BR: Beam Reducer; DM: Dichroic Mirror; S: Safety Shutter; BD: Beam Dump; UPM: Ultrafast Pulse Measurer; ns PD: nanosecond Photodiode; $\lambda/2$: Half-Wave Plate. **B**, Side view of the entire system. **C**, **D**, Detailed pictures of the beam routing components added. **E**, Graph showing intensity of SFG signal excited by wavelength mixing in KDP crystals [18] vs. delay line length variation (Δx), where $\Delta x = 0$ corresponds to the retroreflector position at temporal synchronization. $\lambda_1 = 870$ nm, $P_1 = 5$ mW, $\lambda_2 = 1230$ nm, $P_2 = 3$ mW. The SFG signal was detected in a narrow emission band between 505 and 515 nm. Insets are SFG images of the KDP crystals acquired at the indicated Δx values, keeping all the other acquisition parameters constant.

InGaAs photodetector (DET10N/M, Thorlabs Inc.; Figure S2). The latter was used for coarse synchronization of the two pulsed beams by feeding its output to a fast oscilloscope (part number HMO3004, Rohde & Schwarz GmbH & Co KG, Munich, Germany; Figure S3). The main transmitted component of each laser beam was aligned by means of a periscope in the multi-photon port of the scan head of the upright Leica SP8 microscope (for a detailed list of optical components, see Supplement 1).

The commercial architecture was endowed with 3 different visible laser lines (488 nm, 532 nm and 635 nm) for one-photon multi-color imaging, 4 internal descanned and 4 external non-descanned detectors. Each detector subsystem was composed of 2 InP/InGaAsP photomultiplier tubes (PMT) and 2 higher sensitivity Hybrid Detectors (HyD), that combine superior sensitivity with a large dynamic range. The microscope was also endowed with a commercial STED module (STED 3X, Leica Microsystem) for 1PE-STED. The STED laser source was a 775 nm high power pulsed picoseconds laser source (Katana 08 HP, Onefive, Zurich, Switzerland). We modified the commercial system to trigger the STED laser with the electronics of the Ti:Sa laser with an intervening adjustable picosecond delayer.

2.2. System alignment for 2PE-STED

The commercial system allowed for automatic alignment of the STED beam and the 635 nm excitation laser. After running the automatic alignment procedure, we manually aligned the two IR pulsed laser beams with the 635 nm beam by inspecting the images of 1 μm multicolor fluorescent beads (T7282, TetraSpeck Microspheres, Thermo Fisher Scientific, Waltham, MA, USA) diluted 1:10 in distilled water (Figure S4). To check the alignment of the IR pulsed beams with the donut-shaped 775 nm STED beam, we used the light reflected off 80 nm gold beads (see Section 3.1). For fine adjustment of the donut position and shape, we relied on a customized feature of the control software that allowed us to move the vortex phase plate in two orthogonal directions within the STED module (for more details about software, customized feature and alignment protocols, see Supplement 1).

2.3. Animals

All animal experimentation was conducted in adherence to the NIH Guide for the Care and Use of Laboratory Animals and recommendations from both ARRIVE and PREPARE guidelines [31,32]. Mice were bred and genotyped at Shanghai Biomodel Organism Science & Technology Development Co., Ltd., Shanghai (China). All experiments were performed under animal production license sxck(Shanghai)2017-010 and animal usage license: sxck(Shanghai)2017-012. Mice were housed in individually ventilated caging systems at a temperature of $21 \pm 2\,°C$, relative humidity of $55 \pm 15\%$ with 50–70 air changes per hour and under controlled (12 : 12 hour) light–dark cycles (7 am–7 pm). Mice had ad libitum access to water and a standard rodent diet. For most experiments, we used adult wild type C57BL6/N mice, both male and female, aged between 8 and 12 weeks. For some experiments we used also transgenic mice, both male and female, aged between 8 and 12 weeks, expressing the calcium (Ca^{2+}) biosensor GCaMP6s in the Rosa26 locus after tamoxifen induction, generated by crossing the Jackson Laboratory strain #024106 (STOCK B6;129S6Gt(ROSA)26Sor$^{tm96(CAG-GCaMP6s)Hze}$/J) with the Cre-deleter strain #008463 (B6.129Gt(ROSA)26Sor$^{tm1(cre/ERT2)Tyj}$/J). For *in vivo* imaging, mice were anesthetized with 2% isoflurane and their temperature was kept at 37 °C by a thermostatically controlled heating pad. Animals were returned to their cages at the end of the imaging session.

2.4. Sample preparation

Phantom sample. We dispersed 1 μm polystyrene beads (Cat. No. C37274, Thermo Fisher Scientific) in a 2% low melting point (LMP) agarose gel (Cat. No. A0576, Sigma-Aldrich/Merck, Darmstadt, Germany). The concentration was determined according to Mie scattering theory [33],

to obtain a tissue-like sample with a scattering coefficient of about $20\,mm^{-1}$ at 850 nm. The goal was to effectively mimic typical scattering properties of most common turbid biological samples [34–36]. The stock solution of 200 nm fluorescent crimson beads (Cat. No. F8806, Thermo Fisher Scientific) was diluted 1:5000 in the turbid gel. The fluorescent beads concentration was adjusted to ensure a sufficient number of well-separated beads at every depth with no vertical overlapping. At this dilution, the fluorescent beads did not affect sample's optical properties. $10\,\mu l$ of the fluid mixture was then placed onto a coverglass and covered with a coverslip until the gel solidified. Depth into the sample was measured with objective z-wide focus as the distance from the first top layer of the sample were beads were detected.

Calibration sample of beads and fixed brain slices. For bead sample preparation, $30\,\mu l$ of 0.1% poly-L-lysine solution (Cat. No. P8920 Sigma-Aldrich/Merck) were spread on a cleaned coverglass and incubated at room temperature for 30 min. The coverglass was then washed three times with MilliQ water and dried with nitrogen. Then, the coverglass was covered with $30\,\mu l$ of a solution containing 200 nm crimson fluorescent beads diluted $1:10^4$ in Dulbecco′s phosphate-buffered saline (DPBS) and the solution was allowed to dry. For brain slice preparation, a mouse was anesthetized with gaseous anesthesia before decapitation. The brain was quickly removed and fixed overnight in ice-cold 4% paraformaldehyde (PFA). The following day, the brain was included in 2% LMP agarose gel and cut in coronal section of thickness comprised between 20 and $130\,\mu m$ using a vibratome (VT1220s, Leica). Brain slices were then laid on the coverglass pre-treated with crimson beads, mounted with prolong gold antifade medium (Cat. No. P36930, Thermo Fisher Scientific), covered with a coverslip and sealed with nail polish. Slice thickness was measured with piezo z-focus as the distance between the beads layer and the top slice layer where brain autofluorescence signal was detected.

Immunostaining. Human HeLa cells plated on a glass coverslip were fixed with 4% PFA in DPBS for 15 min, washed 3 times with DPBS and incubated for 30 min at room temperature with blocking buffer (3% bovine serum albumin and 0.1% Triton-X-100 in DPBS). Cells were then incubated for 1 h at room temperature with a monoclonal mouse Anti-Tom20 antibody (1:500, Cat. No. MABT166, Merck & Co., Kenilworth, NJ). The primary antibody was revealed with Atto 594 goat anti-mouse IgG (1:500, Cat. No. 76085-1ML-F, Merck & Co.). The coverslips were rinsed in DPBS, mounted with prolong gold antifade medium (Cat. No. P36930, Thermo Fisher Scientific) and sealed with nail polish.

Tissue sample preparation. Mice were culled by trained personnel using gaseous anesthesia followed by a rising concentration of CO_2 and cervical dislocation to confirm death. For slice preparations of brain and kidney, each organ was explanted, quickly immersed in ice-cold DPBS and free-hand cut in about 1 mm slices. Freshly excited slices were incubated for 30 min at 37°C in a solution of Nile Red (Cat. No. 72485-100MG, Sigma-Aldrich/Merck) pre-dissolved in methanol at a concentration of 1 mg/ml and diluted 1:20 in DPBS. For skin specimens, we followed the protocol described in Ref. [37]. Shortly, a portion of dorsal skin comprising both epidermal and dermal layers (about $1\,cm \times 1\,cm$) was excised and residual hair was removed by using a hair removal cream. The organotypic skin culture was then maintained in a Trowell-type system, with the dermal side immersed in DMEM/F12 supplemented with 10% FBS and the stratum corneum exposed to air. The tissue was stained by applying a $400\,\mu l$ drop of Nile Red 1 mg/ml diluted in methanol and incubated at 37°C for 30 min. The surface was then cleaned with ethanol and rinsed with DPBS. After staining, samples were transferred under the microscope objective and imaged at room temperature for a maximum of 2 hours.

***In vivo* Nile Red staining of the earlobe skin.** After anesthetizing the animal, one of its earlobes was attached on the sample holder with double sided tape. Next, a $30\,\mu l$ drop of Nile Red 1 mg/ml diluted in methanol was applied on the earlobe surface for 5 minutes. Finally, excess solution was gently removed with a cotton swab and the skin surface was cleaned with ethanol and rinsed with DPBS.

2.5. Image acquisition and analysis

Throughout this article, λ denotes the wavelength of the laser beam propagating in empty space (unless otherwise stated). For STED imaging experiments, we define λ_{1P} and λ_{2P} as the excitation wavelength for 1PE and 2PE process, respectively. STED wavelength was fixed at $\lambda_{STED} = 775$ nm. P_{1P}, P_{2P} and P_{STED} denote, respectively, the average 1P excitation, 2P excitation and STED laser power measured at the objective back focal aperture. All images were acquired using the Leica Application Suite X Software. Fluorescence images were acquired with a 63 × glycerol immersion objective (HC PL APO CS2 63×/1.30GLYC) with 1.30 numerical aperture (NA). Unless otherwise stated, the pixel dwell time was 1.95 μs and each image was obtained by line averaging 32 times.

For wavelength mixing experiments, we define λ_1 and λ_2 as the Ti:Sa and OPO excitation wavelength, respectively. P_1 and P_2 denote excitation power measured at the objective back focal aperture for λ_1 and λ_2, respectively. To acquire SFG, SHG, 2c-2PEFM, CARS and multimodal images, we used a 25 × water immersion objective (HC IRAPO L 25×/1.0 W motCORR), the pixel dwell time was 122.4 ns and each image was obtained by averaging 40 consecutive frames, unless otherwise stated.

Image processing was performed offline with the open-source software ImageJ/Fiji (ImageJ-win64). MATLAB (R2019a, The MathWorks, Inc., Natick, MA) was used for data extraction, analysis and fitting.

For the characterization of the full width half maximum (FWHM) of the PSF, for each bead we extracted and averaged the line profile intensity of four independent diameters and fitted the mean profile with a Gaussian function. Reported FWHM values are the average of n ≥5 beads for each depth within the sample. Error bars represent the standard error of the mean.

3. Results and discussion

3.1. Design, construction, spatial and temporal alignment of the multimodal optical architecture

To maximize the versatility of the commercial microscope by adding multimodal capabilities, we modified the system as shown in the scheme of Fig. 1(A). An overview of the system is presented in Fig. 1(B). The OPO provided two laser beams, each pulsed at 80 MHz: the Ti:Sa beam (680-1080 nm) and the OPO beam (1000-1340 nm). For spatial alignment of the two IR excitation sources, we rerouted the OPO beam by introducing two piezo kinematic mirrors in its optical path (Fig. 1(C)), which allowed us to maintain spatial alignment via remote controls (Figure S1). To compensate for the nanosecond temporal delay between the pulses of the two beams, we inserted a software controlled motorized optical delay line in the Ti:Sa path (Fig. 1(D)). To control beam divergence and to compensate for the extra length introduced by the delay line, we also inserted a 1.2 × beam expander. The Ti:Sa and OPO beams merged at a 1035 nm dichroic mirror, followed by a Glan polarizing prism used to divert a fraction of the light towards a beam profiler and a fast photodiode.

For each beam, the fraction of diverted light was determined by the orientation of a motorized half-wave plate preceding the beam-merging dichroic mirror. By adjusting the delay line length while monitoring the fast photodiode output, we synchronized coarsely the two IR pulsed beams at microscope input. Finer synchronization was achieved by focusing the objective on Potassium Dihydrogen Phosphate (KDP, J. T. Backer, Center Valley, PA) crystals while further adjusting the delay line length to maximize the SFG signal elicited by the wavelength mixing phenomenon [18] (Fig. 1(E)). The smoothness of the operation was guaranteed by sub-micrometric computer control of the motorized delay line. To compensate for the wavelength-dependent delay due to the GDD of all the optical elements along the beam path, we performed the synchronization procedure for each Ti:Sa and OPO wavelength combination.

A major goal for this project was to perform 2PE-STED. To this end, we triggered the 775 nm pulsed STED laser by means of the TTL output of the pulsed Ti:Sa source (after synchronizing the Ti:Sa and OPO pulses). A picosecond delayer was used to adjust the timing of the STED pulses relative to the Ti:Sa pulses.

To check the spatial alignment of the Ti:Sa beam with the beam emerging from the 3D STED module, we used 80 nm gold beads plated on a microscope slide mounted on the Super Z Galvo stage. To obtain the *x-y* projection of the PSF, beads where imaged while performing standard raster scanning in the focal plane. To obtain a projection of the PSF in a plane that contained the optical axis, the stage was vibrated in the z-direction while performing fast line scans across the bead. The results of the alignment for both 1PE-STED and 2PE-STED are displayed in Fig. 2. Image quantification yielded the resolution values in Table 1.
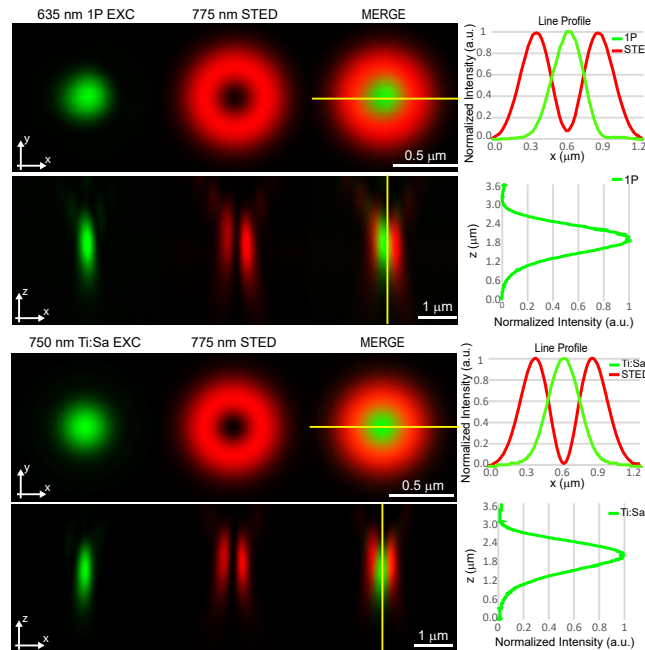
Fig. 2. PSF characterization by means of beam reflection off of 80 nm gold beads. *x-y* and *x-z* projections of the circularly symmetrized excitation (green) and STED (red) beam PSFs for single photon beam at 635 nm (1P EXC, top) and Ti:Sa beam at 750 nm (Ti:Sa EXC, bottom). Right: graphs of the normalized intensity profiles measured along the yellow lines traced on the merge images.

Table 1. FWHM of the measured PSFs in the *x-y* and *x-z* plane

	PSF size (nm)	
	1P EXC	Ti:Sa EXC
x-y	282 ± 2	311 ± 6
x-z	889 ± 9	1105 ± 20

Table 2. FWHM of the PSFs for 2PE and 2PE-STED[a]

	PSF size (nm)		p-value
Depth	2PE	2PE-STED	
0 μm	376 ± 11	193.0 ± 7.5	3.2×10^{-6}
25 μm	377.9 ± 3.8	197 ± 13	4.1×10^{-5}
50 μm	378.9 ± 4.5	202 ± 12	6.6×10^{-7}
75 μm	377.9 ± 3.8	205 ± 16	9.5×10^{-7}
100 μm	401.8 ± 2.9	218 ± 15	2.0×10^{-6}
150 μm	402.6 ± 2.1	229.7 ± 8.5	7.9×10^{-12}
200 μm	404.3 ± 9.9	262 ± 27	5.6×10^{-4}
250 μm	434.5 ± 2.0	303 ± 12	2.7×10^{-7}
300 μm	434.4 ± 7.5	322 ± 18	3.6×10^{-4}

[a]Mean values of the 2PE and 2PE-STED FWHM assessed on 200 nm crimson bead at different depths in the phantom sample. p-values were calculated with two-tailed t-test.

3.2. Characterization of the 2PE-STED performance at increasing depth in thick scattering samples

Since the key novelty of 2PE-STED is the possibility to perform super-resolution imaging deep in turbid biological sample, we tested the capability of our system by assessing the 2PE and 2PE-STED effective PSF as a function of depth in a calibration phantom sample with tissue-like scattering properties.

For the phantom sample, we diluted a given amount of non-fluorescent polystyrene beads in 2% agarose gel [36] to obtain a sample with a scattering coefficient of about 20 mm^{-1}, to mimic the scattering properties of most typical biological tissues [34,35,38]. To assess the resolution performance, we imaged 200 nm crimson beads dispersed in the turbid gel at different depths. Even if these beads are obviously too large to evaluate the best resolution achievable with 2PE-STED, their high brightness and photo-stability make them ideal for 2P-STED imaging deep in a scattering sample [29]. Bead size was small enough to measure the resolution improvement provided by 2PE-STED up to 300 μm of depth (objective working distance). Figure 3(A) shows that, as expected [39], 2PE lateral resolution remained almost constant up to 100 μm, with a significant increase at 250 μm of depth, whereas 2PE-STED FWHM monotonically increased with depth and became significantly wider than the FWHM measured at the sample surface at 100 μm (see Table 2). This was most likely due to spherical aberrations that, by affecting the quality of the STED beam, reduced resolution performance and determined a non-zero donut center that de-excites central fluorescence [29]. This hypothesis is supported by the fact that in our experiments 2PE-STED imaging required a significantly higher enhancement of excitation power at increasing depths, compared to the one required by 2PE imaging.

As shown in Fig. 3(B), we also quantified the resolution improvement provided by 2PE-STED, defined as $\frac{FWHM_{2PE} - FWHM_{2PE-STED}}{FWHM_{2PE}}$%. The resolution improvement was about 50% on the surface and still higher than 25% at maximum depth, ensuring 322 nm resolution 300 μm deep in a turbid media.

Since 2PE-STED was mainly used to distinguish fine structures of synapses or glial cells in the brain [22–25], we also tested the resolution performances of our system by imaging 200 nm crimson beads through fixed brain slices of different thickness (from 20 to 130 μm, Figure S5). Also in this case, the 2PE FWHM remained constant up to 80 μm, while 2PE-STED lateral resolution started to increase at 40 μm of depth. As shown in Figure S5(B), the resolution increment was still higher than 40% at the maximum thickness (130 μm). The intensity line
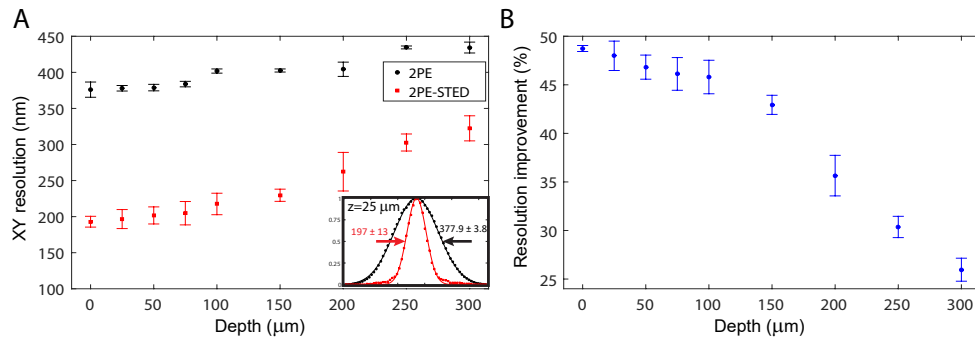
Fig. 3. 2PE and 2PE-STED lateral resolution in a scattering phantom sample as a function of depth. **A**. Evolution of the averaged 2PE (black circles) and 2PE-STED (red squares) FWHM with depth. Inset shows the normalized fluorescence intensity line profile extracted from a 2PE and a 2PE-STED image of a bead at 25 µm of depth. Solid lines are the Gaussian fit of the data; arrows indicate the FWHM of curves; numbers refer to the average 2PE and 2PE-STED FWHM at 25 µm of depth. **B**. Resolution improvement due the application of STED principle to 2PE as function of depth.

profiles reported in Fig. 4 indicate that 2PE-STED imaging allowed to discriminate small structures that were not resolved in 2PE images, making this system valuable for high-resolution imaging deep in the brain. Note that the minimum 2PE-STED FWHM measured was smaller than the declared bead size. This effect was probably due to evaporation and consequent beads shrinking during bead sample preparation.
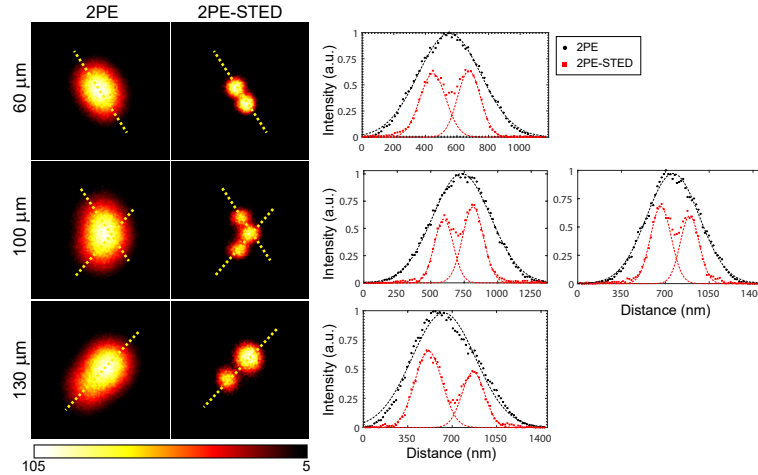
Fig. 4. Comparison between 2PE and 2PE-STED images of fluorescent bead aggregates, imaged through brain slices of different thickness. Left panel, from top to bottom: 2PE and 2PE-STED images of 200 nm crimson beads below brain slices of 60 µm, 100 µm and 130 µm of thickness. λ_{2P} = 850 nm; fluorescence acquisition band = 635-675 nm. Image field of view = 1.63 µm. Right panel: intensity profiles along the dashed yellow lines superimposed on the corresponding images on the left. Solid lines are the best Gaussian fit for each line profile (single or double Gaussian fit for 2PE and 2PE-STED data, respectively). For each thickness, data were normalized to 2PE intensity maximum.

3.3. 2PE-STED imaging on biological samples

To test the super-resolution performances of the temporally and spatially aligned system on stained biological samples, we first used a fixed sample of HeLa cell mitochondria labelled with an anti-Tom 20 antibody counterstained with Atto 594 (Fig. 5). With this type of specimen, there was no advantage of using the 2PE-STED configuration compared to the ordinary 1PE-STED configuration.
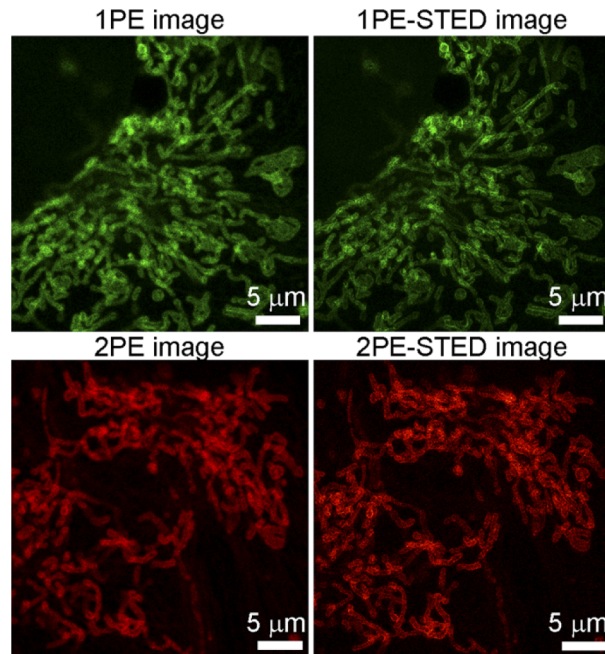

Fig. 5. Comparison between 1PE-STED and 2PE-STED images of fixed HeLa cell mitochondria stained with Atto 594. $\lambda_{1P} = 532$ nm, $P_{1P} = 10\,\mu$W; $\lambda_{2P} = 850$ nm, $P_{2P} = 15$ mW; $P_{STED} = 45$ mW; fluorescence signal was acquired from 630 nm to 690 nm; pixel size = 45 nm; pixel dwell time = 2.4 µs.
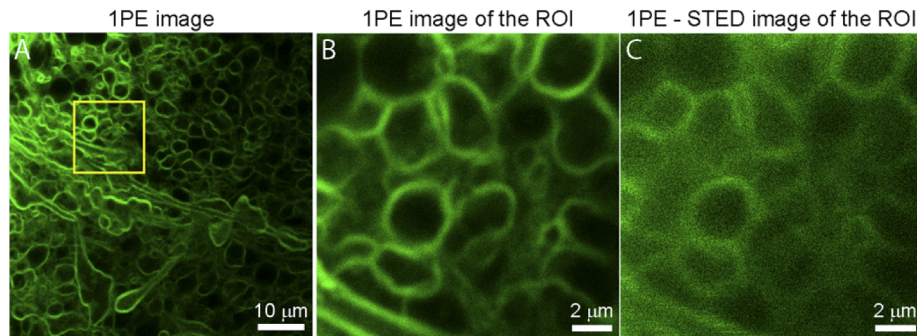
Fig. 6. 1PE and 1PE-STED fluorescence images of myelinated structures in freshly excised mouse brain slice stained with Nile Red, acquired at 20 µm of depth in a wide collection band from 550 nm to 700 nm. $\lambda_{1P} = 532$ nm, $P_{1P} = 15\mu$W; $P_{STED} = 42$ mW; pixel size: 90 nm (**A**) and 18 nm (**B**, **C**).

However, things changed drastically as soon as sample thickness exceeded few tens of microns, as we demonstrated by imaging freshly dissected mouse brain slices stained with Nile Red, a fluorescent hydrophobic dye that quickly and efficiently labels lipid structures and exhibits fluorescence only in a lipid environment [40]. By imaging myelinated structures in the white matter [41], we observed that activating the STED beam in the 1PE-STED configuration caused loss of contrast, resulting in a blurred and poorly resolved image (Fig. 6).

In contrast, activating the STED beam while performing 2PEFM on the same brain sample, at the same depth and STED power, visibly improved both contrast and resolution (Fig. 7). Of note, Nile Red-stained beads were used to characterize the performance of the first 2PE-STED microscope [20].

To evaluate the resolution improvement, we analyzed the pixel intensity profile along selected lines intercepting fine structures of different freshly dissected samples (brain, kidney and
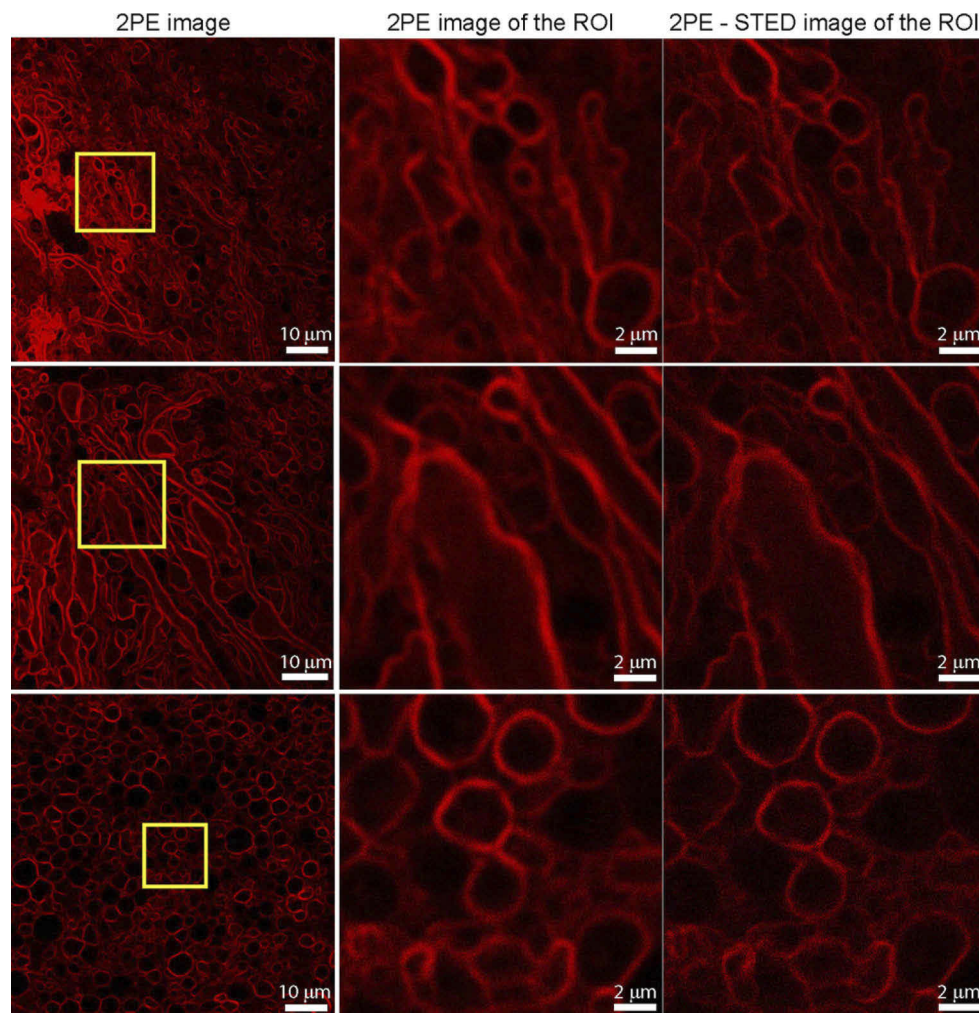

Fig. 7. 2PE and 2PE-STED fluorescence images of myelinated structures at 20 μm of depth in freshly excised white matter of mouse brain slices stained with Nile Red. $\lambda_{2P} = 920$ nm, $P_{2P} = 20$ mW; $P_{STED} = 42$ mW; fluorescence acquisition band = 550-700 nm; pixel size = 90 nm (first column) and 18 nm (all other images).

epidermis) labelled with Nile Red (Fig. 8; images acquired at depths comprised between 20 μm and 60 μm).

By combining 2PE-STED and SHG, we were also able to image Nile Red-stained sebaceous glands nested in dermal collagen fibers both *in vivo* and in freshly excited mouse skin, at depths of 60 μm to 80 μm (Fig. 9). To acquire images deep in the skin, the laser GDD was optimized to maximize fluorescence and SHG signal excitation efficiency, minimizing laser power, acquisition time and tissue damage.

3.4.   *In vivo label-free imaging of skin structures*

To further expand the capabilities of the system, we used additional optical components to exploit non-linear optical phenomena such as 2c-2PEM and CARS microscopy. Key for these applications is the fact that the OPO not only extends the excitation wavelength range of the Ti:Sa laser, but it can also be used to generate non-linear phenomena, based on the spatio-temporal alignment of the two excitation laser beams (as mentioned in the Introduction).

In particular, to use non-linear processes on our platform, we set the Ti:Sa laser at $\lambda_1 = 840$ nm and the OPO at $\lambda_2 = 1105$ nm to image the earlobe skin of live anesthetized mice ubiquitously expressing the green-fluorescent GCaMP6s indicator. With this wavelength combination, the system concurrently allowed us to (i) generate SHG signals from dermal collagen; (ii) visualize GCaMP6s fluorescence in keratinocytes and blood vessels by 2c-2PEFM, according to the equation $\lambda_{2c\text{-}2PE} = 2 \cdot (\lambda_1^{-1} + \lambda_2^{-1})^{-1} \approx 954$ nm [18]; (iii) perform label-free imaging of sebocytes in sebaceous glands (Fig. 10), as well as of subdermal fat in adipose tissue (Fig. 11) as a result of CARS. Note that, as mentioned in the Methods section, λ denotes the free-space wavelength
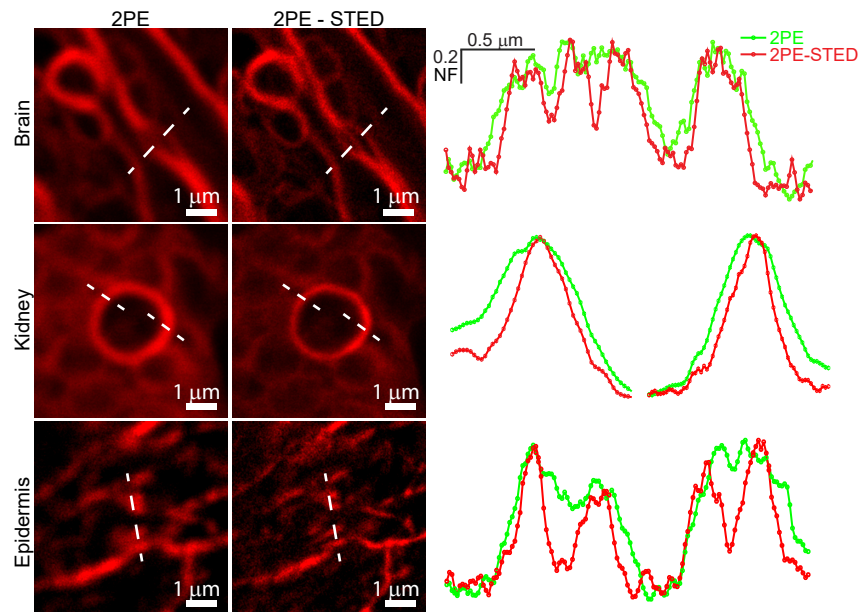

Fig. 8. Resolution improvement due to 2PE-STED microscopy of fine structures in *ex vivo* tissues stained with Nile Red at depths comprised between 20 μm and 60 μm. Images on the left refer to 2PE and 2PE-STED of lipid structures in brain, kidney and epidermis samples. Graphs on the right are corresponding intensity profiles along the white dashed lines drown on the images at left, showing resolution improvement. $\lambda_{2P} = 920$ nm, $P_{2P} = 23$ mW; $P_{STED} = 42$ mW; fluorescence detection band: 550-700 nm; pixel size = 18 nm.
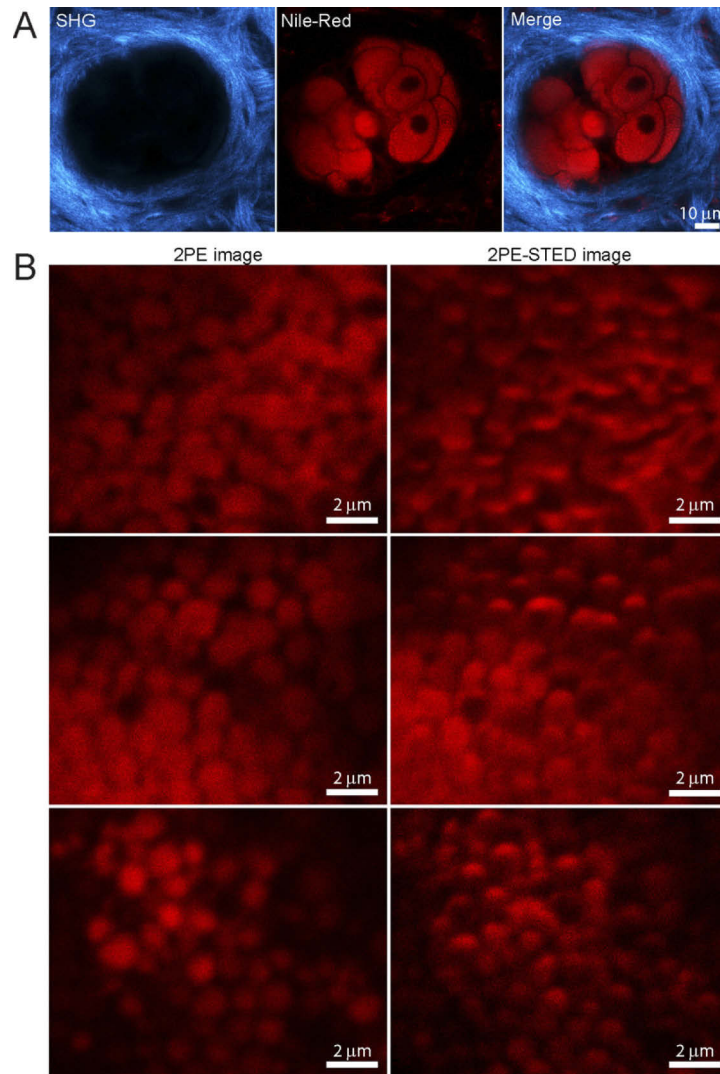
Fig. 9. High-resolution imaging of sebaceous glands by 2PE-STED microscopy. **A**, Representative image of the *x-y* optical section of a Nile Red-stained sebaceous gland more than 70 µm deep in the earlobe skin of a live mouse. SHG signal from collagen fibers is shown in cyan. Images were acquired using a 25 × water immersion objective at an excitation wavelength of 1080 nm; each image is the average of 20 consecutive frames. $P_{2P} = 10$ mW; pixel size =310 nm. Pixel dwell time = 1.367 µs. **B**, Comparison between 2PE and 2PE-STED images of sebocytes acquired 90 µm deep in mouse dorsal skin. Images were acquired with a pixel dwell time of 600 ns and averaging 32 consecutive frames. $\lambda_{2P} = 920$ nm, $P_{2P} = 29$ mW; $P_{STED} = 52$ mW; fluorescence detection band: 550-700 nm; pixel size = 18 nm.

whereas the corresponding wavelength in the tissue is unknown because we did not measure the refractive index of the tissue and its dispersion relations.

To confirm that the observed signals were generated by non-linear effects due to wavelengths mixing, we checked that signals disappeared when exciting the sample only with λ_1 or with λ_2
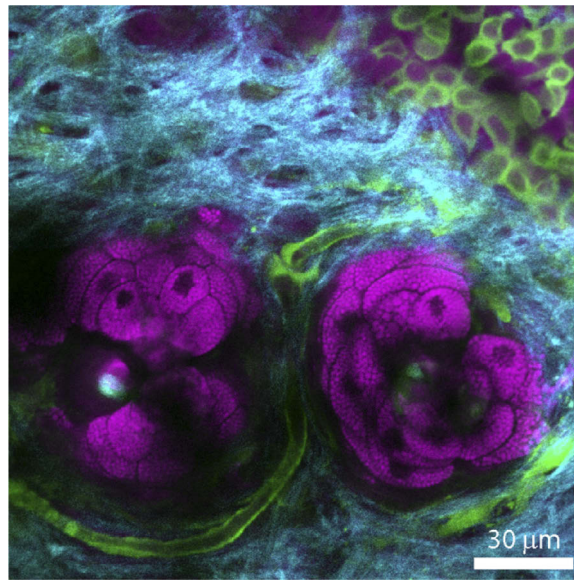
Fig. 10. Combined SHG (cyan), GCaMP6s fluorescence (green) and epi-CARS (magenta) *in vivo* imaging of mouse earlobe skin showing, respectively, collagen, keratinocytes plus blood vessels, and sebocytes of sebaceous glands. $\lambda_1 = 840$ nm, $P_1 = 12$ mW, $\lambda_2 = 1105$ nm, $P_2 = 15$ mW. The SHG signal was collected around 420 nm; the GCaMP6s 2c-2PE fluorescence signal was collected from 505 nm to 545 nm; the CARS signal was collected around 678 nm; pixel size = 192 nm.

(Figure S6). In addition, we also verified that varying both λ_1 and λ_2 resulted in the shifting of the output signal according to the equation $\lambda_{\text{CARS}} = (2\lambda_1^{-1} - \lambda_2^{-1})^{-1}$ (Figure S7).

The possibility to generate 2c-2PEF and CARS signals strongly depended on the inter-pulse delay Δt between Ti:Sa and OPO pulse trains, as demonstrated in Figure S8, where images were acquired while varying Δt from -1 ps to 1 ps. 2c-2PEF and CARS signals failed to be efficiently elicited when the delay between the pulses exceeded 0.16 ps.

CARS imaging highlighted also dermal vasculature and flowing erythrocytes with high resolution and contrast (Fig. 12), suggesting that this label-free imaging modality can be used to quantitatively evaluate blood flow at the level of individual capillaries. Of note, image acquisition at 11 fps showed that the erythrocytes flow was not constant during observation (see Visualization 1 in the Supplementary Material). This approach is highly valuable, for example, to monitor mouse health state during long imaging sessions in a non-invasive label-free manner, therefore maintaining the anesthetized animal close to physiological conditions to preserve experimental outcome and animal welfare [42].

The optical platform presented here is beneficial to all applications that require to simultaneously extract morphological, structural, chemical and molecular information with minimum invasiveness and high spatial and temporal resolution [43]. By combining non-linear excitation processes and upright configuration, our system was proved to be efficiently used to image a variety of thick biological samples, from *ex vivo* tissues to *in vivo* animal models.

We mainly used the platform to investigate morphology [37] and physiological Ca^{2+} signaling [44] in the mouse skin. As shown above, each skin component can be imaged using a different microscopy technique based on its specific composition. In particular, we monitored spontaneous and/or stimulated Ca^{2+} activity (imaged by 2c-2PEF) of basal keratinocytes above collagen fiber layer (imaged by SHG) and in close proximity of sebocytes (imaged by CARS) in the earlobe
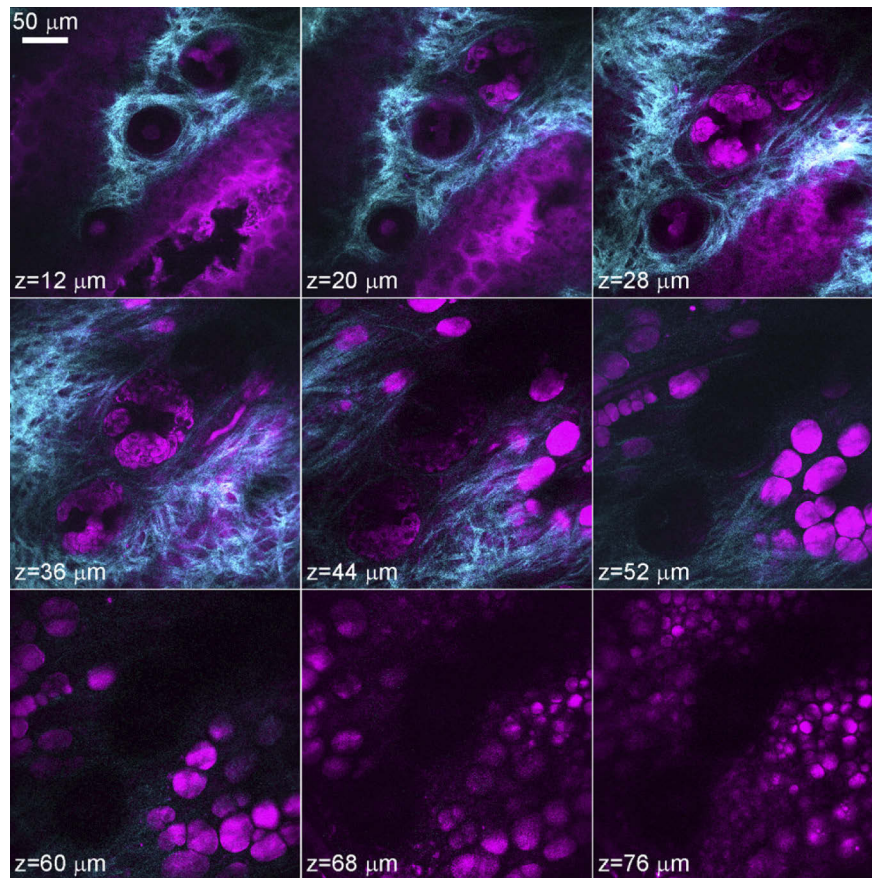
Fig. 11. Through-focus image sequence combining SHG (cyan) and epi-CARS (magenta) *in vivo* signals of unstained wild type mouse earlobe skin showing collagen fibers, keratinocytes, sebocytes of sebaceous glands, blood vessels and lipid droplets of the adipose tissue. Pixel size = 309 nm; other parameters as in Fig. 10.
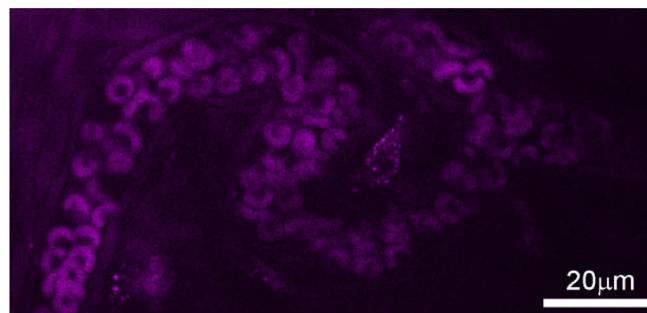

Fig. 12. CARS imaging of flowing erythrocytes in an earlobe capillary of a living mouse. The image was acquired using $\lambda_1 = 840$ nm, $\lambda_2 = 1105$ nm, $P_1 = 12$ mW, $P_2 = 22$ mW. CARS signal was acquired around 678 nm; pixel size = 219 nm. The image was obtained by averaging 11 consecutive video frames (see Visualization 1).

in vivo. By adding proper labelling and switching to 2PE-STED modality, it is also possible to resolve morphological (Fig. 8–9) and possibly functional skin features [28], that are not detectable

by conventional microscopy. Providing information about cell signaling together with a wide description of the tissue, this approach is particularly suitable for the study of the pathophysiology of skin affected by genodermatoses [45] or other diseases [46]. Moreover, intravital microscopy techniques are valuable tools to investigate the effect of specific drugs or therapies on tissues or organs with subcellular resolution. For example, we applied the described optical architecture to investigate in real time molecular processes (interorganellar Ca^{2+} transfer from the endoplasmic reticulum to mitochondria, reactive oxygen species production, caspase activation. . .) elicited by photodynamic therapy in laser-irradiated murine melanoma masses [47]. Label-free studies of processes such as cancer cell migration, tissue invasion and tumor-stromal interactions are only some examples of possible applications of this versatile multimodal microscope. In fact, due to their lipid-rich cell membrane and lipid-poor nuclei membrane, cancer cells generate strong CARS contrast [15] and often migrate along blood vessels or collagen fibers [48,49], that are visible exploiting SHG and THG or auto-fluorescence signals.

3D imaging of thick tissues with minimum manipulation can also be an asset for the development of tissue scaffolds for organogenesis in the biomedical engineering field. By combining cell signaling recordings to morphological/chemical description of the sample [50], it is possible to extract a tissue "fingerprint" to evaluate the quality of the engineered tissues in mimicking structural and functional properties of real tissues [51].

Our multimodal approach could have wide application also in neuroscience, for example on neurological diseases related to white matter demyelination. White matter is enriched in lipidic myelin sheath that can be imaged in a label-free manner by CARS [52] or, after staining, by STED microscopy (Fig. 7–8). The integration of different imaging methods allows direct visualization of white matter together with astrocytes processes and microtubules (imaged with SHG) [53] and Ca^{2+} signaling (imaged with 2PE or 2c-2PE) using a suitable fluorescent sensor [54]. The analysis of interactions between different components of biological systems is crucial to gain insight on disease pathways and could pave the way for future therapeutic approaches.

4. Conclusions

The results presented above demonstrate that a relatively modest investment in terms of additional equipment can substantially improve and expand the performances of a commercial multiphoton/STED architecture. Moreover, the described multimodal imaging platform has the added benefit to be suitable also for non-expert users thanks to the possibility to perform remote system alignment of critical opto-mechanical components.

The key points that allowed us to meet our goals were: i) the addition of the delay line with computer-controlled sub-micrometer precision and related optics to compensate for the nanosecond delay between Ti:Sa and OPO pulses, as well as Ti:Sa beam divergence; ii) the insertion of high-precision remotely-controlled beam-steering mirrors for accurate spatial alignment of Ti:Sa, OPO and STED beams; iii) the customized feature of the control software that allowed us to move the vortex phase plate in two orthogonal directions within the commercial STED module; iv) the picosecond delayer electronics for accurate timing of the STED pulses relative to the Ti:Sa clock. The added benefits include not only the possibility to perform 2PE-STED microscopy at a depth of 300 µm in a scattering tissue-like sample and of 70 µm in skin, but also 2c-2PEF simultaneously with label-free imaging deep in tissues to visualize structures and fast dynamic processes *in vivo*.

The integration of multiple imaging modalities on the same system allows a comprehensive investigation of the sample by simultaneous observation of its different components as well as their interaction, providing a valuable asset for biomedical research.

References

1. N. Mazumder, N. K. Balla, G.-Y. Zhuo, Y. V. Kistenev, R. Kumar, F.-J. Kao, S. Brasselet, V. V. Nikolaev, and N. A. Krivova, "Label-Free Non-linear Multimodal Optical Microscopy—Basics, Development, and Applications," Front. Phys. **7**, 170 (2019).
2. W. Denk, J. H. Strickler, and W. W. Webb, "Two-photon laser scanning fluorescence microscopy," Science **248**(4951), 73–76 (1990).
3. R. Gauderon, P. B. Lukins, and C. J. Sheppard, "Three-dimensional second-harmonic generation imaging with femtosecond laser pulses," Opt. Lett. **23**(15), 1209–1211 (1998).
4. J. Squier, M. Muller, G. Brakenhoff, and K. R. Wilson, "Third harmonic generation microscopy," Opt. Express **3**(9), 315–324 (1998).
5. F. Helmchen and W. Denk, "Deep tissue two-photon microscopy," Nat. Methods **2**(12), 932–940 (2005).
6. W. R. Zipfel, R. M. Williams, and W. W. Webb, "Nonlinear magic: multiphoton microscopy in the biosciences," Nat. Biotechnol. **21**(11), 1369–1377 (2003).
7. V. Parodi, E. Jacchetti, R. Osellame, G. Cerullo, D. Polli, and M. T. Raimondi, "Nonlinear Optical Microscopy: From Fundamentals to Applications in Live Bioimaging," Front. Bioeng. Biotechnol. **8**, 1174 (2020).
8. J. H. Lee, J. J. Rico-Jimenez, C. Zhang, A. Alex, E. J. Chaney, R. Barkalifa, D. R. Spillman Jr., M. Marjanovic, Z. Arp, S. R. Hood, and S. A. Boppart, "Simultaneous label-free autofluorescence and multi-harmonic imaging reveals in vivo structural and metabolic changes in murine skin," Biomed. Opt. Express **10**(10), 5431–5444 (2019).
9. B. E. A. Saleh and M. C. Teich, *Fundamentals of Photonics* (Wiley Interscience, 2007).
10. P. Campagnola, "Second harmonic generation imaging microscopy: applications to diseases diagnostics," Anal. Chem. **83**(9), 3224–3231 (2011).
11. P. Bianchini and A. Diaspro, "Three-dimensional (3D) backward and forward second harmonic generation (SHG) microscopy of biological tissues," J. Biophotonics **1**(6), 443–450 (2008).
12. N. V. Kuzmin, P. Wesseling, P. C. Hamer, D. P. Noske, G. D. Galgano, H. D. Mansvelder, J. C. Baayen, and M. L. Groot, "Third harmonic generation imaging for fast, label-free pathology of human brain tumors," Biomed. Opt. Express **7**(5), 1889–1904 (2016).
13. T. Y. Tsang, "Optical third-harmonic generation at interfaces," Phys. Rev. A **52**(5), 4116–4125 (1995).
14. W. Min, C. W. Freudiger, S. Lu, and X. S. Xie, "Coherent nonlinear optical imaging: beyond fluorescence microscopy," Annu. Rev. Phys. Chem. **62**(1), 507–530 (2011).
15. C. L. Evans and X. S. Xie, "Coherent anti-stokes Raman scattering microscopy: chemical imaging for biology and medicine," Annual Rev. Anal. Chem. **1**(1), 883–909 (2008).
16. D. Kobat, N. G. Horton, and C. Xu, "In vivo two-photon microscopy to 1.6-mm depth in mouse cortex," J. Biomed. Opt. **16**(10), 106014 (2011).
17. P. T. So, C. Y. Dong, B. R. Masters, and K. M. Berland, "Two-photon excitation fluorescence microscopy," Annu. Rev. Biomed. Eng. **2**(1), 399–429 (2000).
18. P. Mahou, M. Zimmerley, K. Loulier, K. S. Matho, G. Labroille, X. Morin, W. Supatto, J. Livet, D. Debarre, and E. Beaurepaire, "Multicolor two-photon tissue imaging by wavelength mixing," Nat. Methods **9**(8), 815–818 (2012).
19. Y. Hontani, F. Xia, and C. Xu, "Multicolor three-photon fluorescence imaging with single-wavelength excitation deep in mouse brain," Sci. Adv. **7**(12), 1 (2021).
20. G. Moneron and S. W. Hell, "Two-photon excitation STED microscopy," Opt. Express **17**(17), 14567–14573 (2009).
21. Q. Li, S. S. Wu, and K. C. Chou, "Subdiffraction-limit two-photon fluorescence microscopy for GFP-tagged cell imaging," Biophys. J. **97**(12), 3224–3228 (2009).
22. K. T. Takasaki, J. B. Ding, and B. L. Sabatini, "Live-cell superresolution imaging by pulsed STED two-photon excitation microscopy," Biophys. J. **104**(4), 770–777 (2013).
23. J. B. Ding, K. T. Takasaki, and B. L. Sabatini, "Supraresolution imaging in brain slices using stimulated-emission depletion two-photon laser scanning microscopy," Neuron **63**(4), 429–437 (2009).
24. P. Bethge, R. Chereau, E. Avignone, G. Marsicano, and U. V. Nagerl, "Two-photon excitation STED microscopy in two colors in acute brain slices," Biophys. J. **104**(4), 778–785 (2013).
25. M. J. T. Ter Veer, T. Pfeiffer, and U. V. Nagerl, "Two-photon STED microscopy for nanoscale imaging of neural morphology in vivo," Methods Mol. Biol. **1663**, 45–64 (2017).
26. I. Coto Hernandez, M. Castello, G. Tortarolo, N. Jowett, A. Diaspro, L. Lanzano, and G. Vicidomini, "Efficient two-photon excitation stimulated emission depletion nanoscope exploiting spatiotemporal information," Neurophotonics **6**(04), 1 (2019).

27. K. Otomo, T. Hibi, Y. C. Fang, J. H. Hung, M. Tsutsumi, R. Kawakami, H. Yokoyama, and T. Nemoto, "Advanced easySTED microscopy based on two-photon excitation by electrical modulations of light pulse wavefronts," Biomed. Opt. Express **9**(6), 2671–2680 (2018).

28. M. G. M. Velasco, M. Zhang, J. Antonello, P. Yuan, E. S. Allgeyer, D. May, O. M'Saad, P. Kidd, A. E. S. Barentine, V. Greco, J. Grutzendler, M. J. Booth, and J. Bewersdorf, "3D super-resolution deep-tissue imaging in living mice," Optica **8**(4), 442–450 (2021).

29. S. Bancelin, L. Mercier, E. Murana, and U. V. Nagerl, "Aberration correction in stimulated emission depletion microscopy to increase imaging depth in living brain tissue," Neurophotonics **8**(03), 035001 (2021).

30. I. Coto Hernandez, M. Castello, L. Lanzano, M. d'Amora, P. Bianchini, A. Diaspro, and G. Vicidomini, "Two-photon excitation STED microscopy with time-gated detection," Sci. Rep. **6**(1), 19419 (2016).

31. C. Kilkenny, W. J. Browne, I. C. Cuthill, M. Emerson, and D. G. Altman, "Improving bioscience research reporting: the ARRIVE guidelines for reporting animal research," PLoS Biol. **8**(6), e1000412 (2010).

32. A. J. Smith, R. E. Clutton, E. Lilley, K. E. A. Hansen, and T. Brattelid, "PREPARE: guidelines for planning animal research and testing," Lab. Anim. **52**(2), 135–141 (2018).

33. S. Prahl, "Mie scattering calculator."

34. W. F. Cheong, S. A. Prahl, and A. J. Welch, "A review of the optical-properties of biological tissues," IEEE J. Quantum Electron. **26**(12), 2166–2185 (1990).

35. M. Lee, E. Lee, J. Jung, H. Yu, K. Kim, J. Yoon, S. Lee, Y. Jeong, and Y. Park, "Label-free optical quantification of structural alterations in Alzheimer's disease," Sci. Rep. **6**(1), 31034 (2016).

36. Z. Lavagnino, F. C. Zanacchi, E. Ronzitti, and A. Diaspro, "Two-photon excitation selective plane illumination microscopy (2PE-SPIM) of highly scattering samples: characterization and application," Opt. Express **21**(5), 5998–6008 (2013).

37. Y. Kuang, V. Zorzi, D. Buratto, G. Ziraldo, F. Mazzarda, C. Peres, C. Nardin, A. M. Salvatore, F. Chiani, F. Scavizzi, M. Raspa, M. Qiang, Y. Chu, X. Shi, Y. Li, L. Liu, Y. Shi, F. Zonta, G. Yang, R. A. Lerner, and F. Mammano, "A potent antagonist antibody targeting connexin hemichannels alleviates Clouston syndrome symptoms in mutant mice," EBioMedicine **57**, 102825 (2020).

38. A. Taddeucci, F. Martelli, M. Barilli, M. Ferrari, and G. Zaccanti, "Optical properties of brain tissue," J. Biomed. Opt. **1**(1), 117–123 (1996).

39. C. Y. Dong, K. Koenig, and P. So, "Characterizing point spread functions of two-photon fluorescence microscopy in turbid medium," J. Biomed. Opt. **8**(3), 450–459 (2003).

40. S. D. Fowler and P. Greenspan, "Application of Nile red, a fluorescent hydrophobic probe, for the detection of neutral lipid deposits in tissue sections: comparison with oil red O," J. Histochem. Cytochem. **33**(8), 833–836 (1985).

41. S. Mollmert, M. A. Kharlamova, T. Hoche, A. V. Taubenberger, S. Abuhattum, V. Kuscha, T. Kurth, M. Brand, and J. Guck, "Zebrafish spinal cord repair is accompanied by transient tissue stiffening," Biophys. J. **118**(2), 448–463 (2020).

42. J. L. Tremoleda, A. Kerton, and W. Gsell, "Anaesthesia and physiological monitoring during in vivo imaging of laboratory rodents: considerations on experimental outcomes and animal welfare," EJNMMI Res. **2**(1), 44 (2012).

43. S. Yue, M. N. Slipchenko, and J. X. Cheng, "Multimodal nonlinear optical microscopy," Laser Photonics Rev. **5**(4), 496–512 (2011).

44. V. Donati, C. Peres, C. Nardin, F. Scavizzi, M. Raspa, C. D. Ciubotaru, M. Bortolozzi, M. G. Pedersen, and F. Mammano, "Calcium signaling in the photodamaged skin: in vivo experiments and mathematical modeling," Function **zqab064** (2021).

45. F. Bosen, M. Schutz, A. Beinhauer, N. Strenzke, T. Franz, and K. Willecke, "The Clouston syndrome mutation connexin30 A88 V leads to hyperproliferation of sebaceous glands and hearing impairments in mice," FEBS Lett. **588**(9), 1795–1801 (2014).

46. R. Cicchi, D. Kapsokalyvas, and F. S. Pavone, "Clinical nonlinear laser imaging of human skin: a review," BioMed Res. Int. **2014**, 1–14 (2014).

47. C. Nardin, C. Peres, S. Putti, T. Orsini, C. Colussi, F. Mazzarda, M. Raspa, F. Scavizzi, A. M. Salvatore, F. Chiani, A. Tettey-Matey, Y. Kuang, G. Yang, M. A. Retamal, and F. Mammano, "Connexin hemichannel activation by S-nitrosoglutathione synergizes strongly with photodynamic therapy potentiating anti-tumor bystander killing," Cancers **13**(20), 5062 (2021).

48. H. Yamaguchi, J. Wyckoff, and J. Condeelis, "Cell migration in tumors," Curr. Opin. Cell Biol. **17**(5), 559–564 (2005).

49. W. J. Han, S. H. Chen, W. Yuan, Q. H. Fan, J. X. Tian, X. C. Wang, L. Q. Chen, X. X. Zhang, W. L. Wei, R. C. Liu, J. L. Qu, Y. Jiao, R. H. Austin, and L. Y. Liu, "Oriented collagen fibers direct tumor cell intravasation," Proc. Natl. Acad. Sci. U. S. A. **113**(40), 11208–11213 (2016).

50. C. C. Moura, K. N. Bourdakos, R. S. Tare, R. O. C. Oreffo, and S. Mahajan, "Live-imaging of bioengineered cartilage tissue using multimodal non-linear molecular imaging," Sci. Rep. **9**(1), 5561 (2019).

51. L. Coluccino, C. Peres, R. Gottardi, P. Bianchini, A. Diaspro, and L. Ceseracciu, "Anisotropy in the viscoelastic response of knee meniscus cartilage," J. Appl. Biomater. Func. **15**(1), 77–83 (2017).

52. H. Wang, Y. Fu, P. Zickmund, R. Shi, and J. X. Cheng, "Coherent anti-stokes Raman scattering imaging of axonal myelin in live spinal tissues," Biophys. J. **89**(1), 581–591 (2005).

53. Y. Fu, H. Wang, R. Shi, and J. X. Cheng, "Second harmonic and sum frequency generation imaging of fibrous astroglial filaments in ex vivo spinal tissues," Biophys. J. **92**(9), 3251–3259 (2007).

54. Y. Fu, H. Wang, T. B. Huff, R. Shi, and J. X. Cheng, "Coherent anti-Stokes Raman scattering imaging of myelin degradation reveals a calcium-dependent pathway in lyso-PtdCho-induced demyelination," J. Neurosci. Res. **85**(13), 2870–2881 (2007).